Bounds on Robustness Limitations for Unstable Aircraft Using the Bode Sensitivity Integral

Jared A. Grauer*
NASA Langley Research Center, Hampton, Virginia, 23681

This paper investigates limitations in achievable robustness of statically unstable aircraft using the Bode sensitivity integral. A previous analysis of the X-29 aircraft is studied, and details about the available bandwidth and robustness limitations are re-examined using high-fidelity linear models of the aircraft and control system. Based on these results, a modified analysis was performed on the X-59 Low-Boom Flight Demonstrator to illustrate the same type of fundamental limitations and difficulties in meeting traditional specifications on gain and phase margins.

Nomenclature

$\mathfrak{I}$ = imaginary part
j = imaginary number, $\sqrt{-1}$
$\mathfrak{R}$ = real part
s = Laplace variable
t = time, s
ω = frequency, rad/s
$|.|$ = absolute value
$\angle$ = angle, rad

Superscripts
^{T} = transpose
$\dot{}$ = time derivative
$\hat{}$ = estimated value

I. Introduction

The National Aeronautics and Space Administration (NASA) and Lockheed Martin are presently developing the X-59 Low-Boom Flight Demonstrator (LBFD) aircraft under the Quiet SuperSonic Technology (QueSST) project [1]. Figure 1(a) shows a photograph of the aircraft. The X-59 was designed to emit a quieter sonic boom, as perceived by observers on the ground, than other supersonic transport aircraft. The project seeks to fly the airplane over U.S. communities, survey public reactions, and inform federal regulators in the U.S. and abroad who may then consider lifting the ban on supersonic flight over land.

Similar to other supersonic aircraft, the X-59 has an aerodynamic center located forward of the center of gravity (CG). This configuration creates a static instability in pitch, and necessitates a flight control system for stabilizing the aircraft and achieving acceptable handling qualities. In addition to the normal difficulties encountered when designing a flight control system (i.e., effects of measurement noise, disturbances, model error, etc.), the control design is further burdened by unique features of the X-59 including a large pitch inertia, low-frequency structural modes, the static instability, and constraints associated with tailoring the sonic boom.

As the fidelity of pre-flight simulation models matured, it became apparent that robustness requirements were difficult to meet in some parts of the desired flight envelope. Initially, these requirements were set to the levels specified of generic military aircraft [2–5]. Because these levels are intended to cover the aircraft lifecycle, an engineering analysis was made to determine lower and more relevant robustness requirements for the X-59 and its mission. This narrative roughly parallels the previous development of the X-29 advanced technology demonstrator, which is pictured

*Research Engineer, Dynamic Systems and Control Branch, MS 308. Associate Fellow AIAA.

(a) X-59 (credit: Lockheed Martin Skunk Works)

(b) X-29B (credit: NASA / Larry Sammons)

Fig. 1 Subject aircraft.

in Fig. 1(b). The X-29 is currently the most unstable fighter-like airplane tested, and also required specification relief from robustness metrics [6–8].

In his presentation "Respect the Unstable" for the first IEEE CSS Hendrik W. Bode Lecture Prize [9, 10], Gunter Stein gave a simple retrospective analysis using the Bode sensitivity integral [11] that showed fundamental limitations in achievable robustness for the X-29 control design due to the static instability of the airframe and bandwidth of the available hardware. He explained how this integral can be viewed as a conservation law for feedback control systems, wherein reduced sensitivity to tracking errors and external disturbances in one frequency range is met with increased sensitivity, and therefore decreased robustness, in another frequency range [12]. About the X-29 control law design, Stein recounts

> . . . and got control laws, and missed the fact that this was almost too unstable to be reasonably controlled against military specs . . . If we had instead done a little Bode integral calculation at the beginning, we would have all agreed: hey, this thing is going to be marginal. Instead, we argued for years — pretty heated arguments among some of the design teams — about what one or the other team wasn't doing right. So it was the lack of understanding of the fundamentals that I'm trying to talk about here today that led us into a lot of unnecessary heartaches.

He further elaborates

> . . . as a result, we're really stuck. And all the various other design groups that finally studied this, with all the tools they could bring to bear, came to that same conclusion. And I've simply done it on the back of an envelope, if you will, with Bode's integral. And again, if we had done that in the first place, we would have saved a lot of arguments . . .

To provide another perspective on the fundamental robustness limitations for the X-59, an effort was undertaken to understand and apply Stein's analysis using the Bode sensitivity integral. In studying the X-29 example, the general insights and numerical values reported in Refs. [9, 10] were confirmed. However, discrepancies were also found that led to incorrect conclusions about a critical parameter in the analysis called the available bandwidth. In order to apply Stein's approach to the X-59, these discrepancies were further studied, and a modified analysis was developed.

This paper summarizes the effort to apply Stein's analysis using the Bode sensitivity integral to the X-59 and assess robustness limitations. The contributions of the paper include an examination of Stein's arguments, a modified version of the analysis, and an assessment of the X-59 robustness limitations. The paper is organized as follows. Section II reviews the nomenclature and theory associated with classical servomechanisms. Section III revisits Stein's analysis of the X-29 and motivates the proposed modifications to that analysis. Section IV applies this modified analysis to the X-59. Section V concludes the paper.

II. Classical Control Theory

This section reviews the relevant fundamentals of classical servomechanism analysis and design. More detail can be found in textbooks on the subject, such as Refs. [12–14]. The convention is taken that lower-case symbols are

time-domain representations of signals, whereas upper-case symbols are representations in the Laplace or frequency domains. For example, a response has the time history $y(t)$, Laplace transform $Y(s)$, and frequency response $Y(j\omega)$. Only linear time-invariant (LTI), single-input single-output (SISO) systems are discussed.

A. Transfer Functions

Figure 2 shows a simplified block diagram of a traditional servomechanism. The block $G(s)$ represents the plant and $H(s)$ represents the control law. The signal $r(t)$ is the reference input, $e(t)$ is the tracking error, $u(t)$ is the control signal, and $y(t)$ is the response.

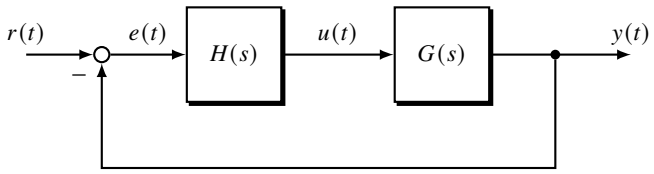

Fig. 2 Block diagram of a traditional servomechanism.

From the open-loop transfer function

$$L(s) = G(s)\,H(s) \tag{1}$$

block-diagram algebra can be used to derive the closed-loop transfer functions

$$S(s) = \frac{E(s)}{R(s)} = \frac{1}{1 + G(s)H(s)} = \frac{1}{1 + L(s)} \tag{2}$$

$$T(s) = \frac{Y(s)}{R(s)} = \frac{G(s)H(s)}{1 + G(s)H(s)} = \frac{L(s)}{1 + L(s)} \tag{3}$$

The tracking error due to a reference input is called the sensitivity transfer function, $S(s)$. The plant response due to a reference command is called the co-sensitivity function, $T(s)$. Equations (2) and (3) are related by the constraint

$$S(s) + T(s) = 1 \tag{4}$$

From Eq. (2), the sensitivity and loop transfer functions are also related by

$$L(s) = \frac{1}{S(s)} - 1 \tag{5}$$

The formulation in Eq. (5) is relevant because on a Nyquist diagram, $1/|S(j\omega)|$ is the relative distance to the critical point $-1 + 0j$, which motivates the stability margin discussed next in Section II.B.

From a loop-shaping perspective, these transfer functions can be characterized in terms of three frequency ranges: low, middle, and high. At low frequencies, a large loop gain is desired to provide good reference tracking and disturbance rejection, which makes $|L(j\omega)|$ large, $|S(j\omega)|$ small, and $|T(j\omega)|$ equal to one. At high frequencies, a small loop gain is desired to desensitize the system to measurement noise and modeling errors, which makes $|L(j\omega)|$ small, $|S(j\omega)|$ equal to one, and $|T(j\omega)|$ small. In the mid-frequency range, the frequency responses need to transition appropriately between these two extremes. According to the Bode gain and phase relationship [12, 15], good robustness is achieved when $|L(j\omega)|$ decreases at about -20 dB/dec in this region, which creates small peaks in $|S(j\omega)|$ and $|T(j\omega)|$.

B. Robustness Metrics

The classical gain and phase margins, as well as the stability margin (sometimes also called the vector margin), are used to quantify robustness. The gain margin, k_m, is the amount of pure gain variation at the phase crossover frequency, ω_{pc}, that can be tolerated before the closed-loop system becomes unstable. Similarly, the phase margin, ϕ_m, is the amount of pure phase variation that can be tolerated at the gain crossover frequency, ω_{gc}, before the closed-loop system becomes unstable. The phase crossover and gain crossover frequencies are where $\angle L(j\omega) = -180$ deg and

where $|L(j\omega)| = 1$, respectively. The merging of these crossover frequencies is the critical point, $s = -1 + 0j$. Typical robustness requirements used in flight control are ±6 dB of gain margin and ±45 deg of phase margin [3].

The utility of gain and phase margins in quantifying the robustness of SISO systems stems from their relationships to physical parameters, such as errors in mass and inertia or unmodeled time delays [16]. Additionally, they provide somewhat orthogonal directions of robustness when viewed as a Nyquist diagram or Nichols chart. However, one major shortcoming of these metrics is that arbitrarily poor robustness due to simultaneous combinations of gain and phase variation is masked. Instead, the stability margin, s_m, can be used to quantify the shortest distance in the complex plane between $L(j\omega)$ and the critical point. In terms of the sensitivity transfer function, the stability margin is

$$s_m = \frac{1}{M_s} \tag{6}$$

where M_s is the maximum or peak value of $|S(j\omega)|$. Typical recommendations for s_m in other aerospace applications vary between $1/2$ (which corresponds to $k_m = 2$ or about 6 dB and $\phi_m = 30$ deg) and $3/4$ (which corresponds to $k_m = 4$ or about 12 dB and $\phi_m = 45$ deg) [17].

The stability margin and the peak sensitivity can be related to the gain and phase margins by the following inequalities [12, 18, 19]

$$k_m \geq \frac{1}{1 - s_m} = \frac{M_s}{M_s - 1} \text{ for } k_m > 1 \tag{7a}$$

$$k_m \leq \frac{1}{1 + s_m} = \frac{M_s}{M_s + 1} \text{ for } k_m < 1 \tag{7b}$$

$$\phi_m \geq 2 \arcsin\left(\frac{s_m}{2}\right) = 2 \arcsin\left(\frac{1}{2M_s}\right) \tag{7c}$$

Note that these are guaranteed lower bounds on the gain and phase margins based on the stability margin or peak sensitivity. The actual gain and phase margins can be significantly higher than these lower bounds. Also note it is not possible to do the reverse and bound s_m and M_s based on k_m and ϕ_m, which again is a shortcoming of using gain and phase margins as metrics for robustness.

Figure 3 shows an example polar plot on the complex plane. The black line is representative of $L(j\omega)$ for the dynamics discussed in this paper. The blue dashed line is the unit circle which passes through the critical point. The red disk is centered at the critical point and has radius s_m, which is the shortest distance between $L(j\omega)$ and the critical point. The green annotations define the two phase crossover points and the gain crossover, as well as their corresponding margins. The negative, lower-frequency gain margin is denoted k_{m_1} and the positive, higher-frequency gain margin is denoted k_{m_2}. The point of this figure is to help illustrate that the inequalities for the gain and phase margins based on s_m in Eq. (7) are lower bounds.

C. Bode Sensitivity Integral

Practically speaking, feedback control designs are compromises between performance and robustness. This trade-off can be quantified by the Bode sensitivity integral, which for a SISO system with $L(s)$ having a relative degree greater than one is

$$\int_0^\infty \ln|S(j\omega)|\, d\omega = \pi \sum_{i=1}^{N_u(L)} \Re\left(p_{u_i}\right) \tag{8}$$

where p_u are the $N_u(L)$ unstable poles of $L(s)$ [11]. Extensions of this integral have been made for cases such as non-minimum phase zeros, time delays, multiple-input multiple-output (MIMO) systems, and others [19–22].

In words, Eq. (8) means that the integral of the sensitivity log magnitude over all frequencies evaluates to a constant. In the limiting case for open-loop stable systems, that constant is zero. For open-loop unstable systems, that constant is a larger value, which depends on the locations of any unstable poles. In any case, decreased sensitivity at low frequencies to meet performance requirements is met with increased sensitivity at higher frequencies, which decreases robustness. This phenomenon is often analogized as the "waterbed effect." In comparison to stable systems, unstable systems have more total sensitivity, so that there is less robustness for the same level of performance. Stein [9] likened this log sensitivity magnitude to "dirt — it's stuff we don't want. We'd rather not have it around. We'd rather get rid of it."

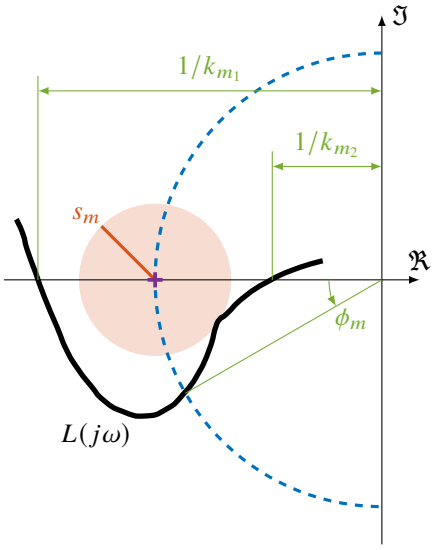

Fig. 3 Representative open-loop polar plot of statically unstable aircraft.

III. Analysis of the X-29 Aircraft

A. Subject Vehicle

Two X-29 airplanes were built by Grumman under funding from the Defense Advanced Research Projects Agency (DARPA) to integrate and demonstrate several advanced technologies such as composite manufacturing, aeroelastic tailoring, digital flight control, and others [23]. NASA and the United States Air Force (USAF) then took ownership of the aircraft and made 374 test flights from 1984 to 1992 before retiring the aircraft. The airplanes are currently on display at NASA Armstrong Flight Research Center (AFRC) in Edwards, CA and at the National Museum of the United States Air Force in Dayton, OH.

The most distinguishing features of the X-29 are the canards and forward-swept wings. This configuration is more efficient than conventional vehicle designs because the extra weight of a horizontal tail is not present, nor is the downward force typically needed to trim the vehicle. However, this configuration also creates a static instability because the aerodynamic center is located forward of the CG for efficient supersonic flight. In the subsonic regime, the instability is even more severe.

The static instability can be understood using the short period mode approximation, which is given by the state-space model [24, 25]

$$\begin{bmatrix} \dot{\alpha}(t) \\ \dot{q}(t) \end{bmatrix} = \begin{bmatrix} Z_\alpha & 1 + Z_q \\ M_\alpha & M_q \end{bmatrix} \begin{bmatrix} \alpha(t) \\ q(t) \end{bmatrix} + \begin{bmatrix} Z_\delta \\ M_\delta \end{bmatrix} \delta(t) \tag{9}$$

The input is a generic control surface deflection δ, and the states are the angle of attack α and pitch rate q. These states and controls represent perturbations away from steady reference values. Terms inside the matrices (e.g., Z_α and M_δ) are the dimensional stability and control derivatives. The canards, symmetric flaps on the trailing edges of the wings, and strake flaps along the aft fuselage are used in pitch control. For conventional aircraft that are statically stable, the roots of the corresponding characteristic equation form a pair of underdamped poles in the left-half plane. For statically unstable aircraft, such as the X-29, the characteristic equation factors as

$$\Delta(s) = (s + p_s)\,(s + p_u) \tag{10}$$

where p_s and p_u are stable and unstable first-order poles, respectively. Such aircraft are conditionally stable, where both increases and decreases in the loop gain lead to instability, which is the reason for the two gain margins.

B. Stein's Analysis

In Refs. [9, 10], Stein idealized the sensitivity function magnitude for the pitch dynamics as the piece-wise continuous straight-line approximations shown on a log-log plot in Fig. 4(a) and given by the equations

$$|S(j\omega)| = \begin{cases} M_s\omega/\Omega_1, & \omega \le \Omega_1 & \text{(11a)} \\ M_s, & \Omega_1 < \omega \le \Omega_a & \text{(11b)} \\ 1, & \Omega_a < \omega & \text{(11c)} \end{cases}$$

The symbol Ω_1 is roughly the largest frequency at which good performance is attained, and is called the performance bandwidth. The symbol Ω_a is the maximum frequency at which the physical system can be controlled as intended and is called the available bandwidth. From a loop-shaping perspective, Fig. 4(a) has the desired general form.

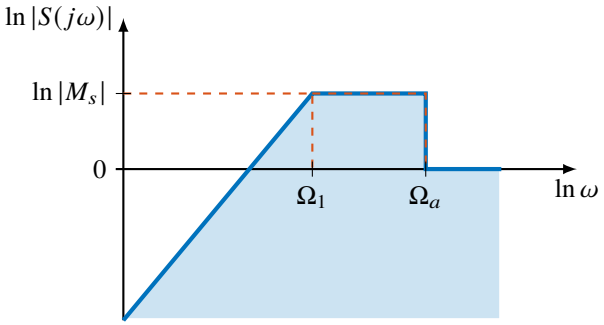

(a) Prototype sensitivity function

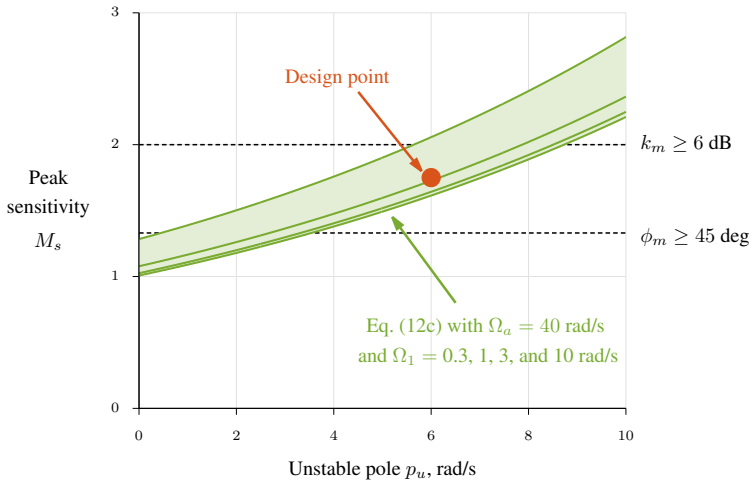

(b) Peak sensitivities

Fig. 4 Analysis of the X-29, adapted from Ref. [10].

Considering the unstable pole from the short period approximation in Eq. (10) and substituting the straight-line approximations of the sensitivity function in Eq. (11) into Eq. (8) allows the Bode sensitivity integral to be written as

$$\int_0^{\Omega_1} \ln\left|\frac{M_s\omega}{\Omega_1}\right| d\omega + \int_{\Omega_1}^{\Omega_a} \ln|M_s|\, d\omega + \int_{\Omega_a}^{\infty} \ln|1|\, d\omega = \pi p_u \tag{12a}$$

Evaluating these integrals results in

$$\Omega_1\,[\ln(M_s) - 1] + (\Omega_a - \Omega_1)\ln(M_s) + 0 = \pi p_u \tag{12b}$$

from which the peak sensitivity can then be solved for as

$$M_s = \exp\left[\frac{\pi p_u + \Omega_1}{\Omega_a}\right] \tag{12c}$$

Equation (12c) is helpful in understanding the fundamental limitations in robustness of unstable systems. This equation quantifies the peak sensitivity (and therefore robustness as defined by the stability margin) as a function of the unstable pole, available bandwidth, and performance bandwidth.

Stein selected four representative values of Ω_1 between 0.3 and 10 rad/s, chose Ω_a as 40 rad/s, and evaluated Eq. (12c) for values of p_u between 0 and 10 rad/s. Figure 4(b) shows results for the peak sensitivities based on these values. The green lines are the four representative curves. From Eq. (12c), Ω_1 acts to shift the curves vertically on the plot whereas Ω_a determines the exponential growth rate. The red circle marker is the design point of the X-29, which was at $p_u = +6$ rad/s and $\Omega_1 = 3$ rad/s [6, 9, 10]. The horizontal lines at 2.0048 and 1.3066 represent the values of M_s where the lower bounds for the gain and phase margins are 6 dB and 45 deg, respectively, based on the inequalities in Eq. (7). Above these lines, it is possible that the inequalities are still met, but there is no guarantee. For a given Ω_a, robustness degrades as Ω_1 increases and/or as the unstable pole moves farther into the right half plane (RHP). Based on this diagram, it was argued in Refs. [9, 10] that it was difficult to get the X-29 to meet the original phase margin requirements at the design point.

C. Linear Models

The remaining analyses presented in this section uses the linear models of the X-29A from Ref. [26]. These models are of relatively high fidelity and include dynamics for the stick shaping, control laws, actuators, rigid-body bare airframe, sensors, filtering, and time delays. The models include one powered approach (PA) configuration at low speed and low altitude, and two up-and-away (UA) configurations at different altitudes and subsonic Mach numbers. Decoupled longitudinal and lateral-directional models at each of these conditions are given for both the normal digital (ND) and the analog reversion (AR) backup control systems.

Table 1 summarizes the flight conditions and control modes for these linear models. Based on the information published in Ref. [26], these models were programmed in MATLAB®* and Simulink® for this study. Each model was then verified against digitized time histories and frequency responses in Refs. [26, 27].

Table 1 Summary of X-29 models in Ref. [26]

Model	Mode	Mach No.	Altitude, ft
1	ND-PA	0.258	4,000
2	AR-PA	0.258	4,000
3	ND-UA	0.70	20,000
4	AR-UA	0.70	20,000
5	ND-UA	0.90	8,000
6	AR-UA	0.90	8,000

As detailed in Refs. [6–8, 26–28], the linear models use different control architectures. Each setup, however, includes proportional-integral (PI) compensation with additional lead networks in the feedback path. The ND-PA configuration is a pitch rate command system using pitch rate and synthesized pitch acceleration. The ND-UA configuration is similar to ND-PA, except that an n_z command system is used with normal acceleration at the pilot station included as a feedback. Both AR-PA and AR-UA use the same simplified architecture, which is again a pitch rate command system with pitch rate being the only feedback. Gains for each configuration are scheduled with the flight condition.

Table 2 lists relevant stability and robustness metrics for the decoupled longitudinal models. The unstable short period poles differ slightly between the ND and AR modes for the same Mach number due to differences in the control systems and differences in trim variables not listed here, such as weight and angle of attack [26]. Every pair of models listed becomes increasingly unstable in the bare-airframe dynamics, which results in less robustness.

D. Reassessing the Source of the Available Bandwidth

In comparing the discussion of the available bandwidth in Refs. [9, 10] with information given in Ref. [26] and other NASA documents (cited below), potential discrepancies arise in how the value of Ω_a was selected as 40 rad/s. To apply

*The use of trademarks or names of manufacturers in this report is for accurate reporting and does not constitute an official endorsement, either expressed or implied, of such products or manufacturers by the National Aeronautics and Space Administration.

Table 2 Stability and robustness metrics for the X-29 linear models

Model	p_u, rad/s	M_s	k_{m_1}, dB	ω_{pc_1}, rad/s	k_{m_2}, dB	ω_{pc_2}, rad/s	ϕ_m, deg	ω_{gc}, rad/s
1	+1.51	1.3	−9.6	0.9	+13.5	31.0	49.2	4.4
2	+1.52	1.3	−6.6	0.8	+20.1	28.9	45.6	3.1
3	+2.86	1.8	−8.6	1.8	+8.1	24.7	45.0	8.8
4	+3.05	1.7	−8.0	1.8	+9.7	31.2	39.2	9.1
5	+5.12	2.7	−6.8	2.9	+5.0	25.9	35.0	14.3
6	+5.18	2.0	−4.3	2.7	+6.4	30.5	35.4	10.9

Stein's simple analysis using the Bode sensitivity integral to other aircraft, it is critical to have a clear understanding in how this parameter is chosen. Mathematically, Ω_a dictates the growth rate of the exponential in Eq. (12c) and has a large effect on the achievable robustness. More intuitively, Ω_a limits the frequency range over which the sensitivity function can be usefully shaped.

Stein examined several sources of potential bandwidth limitation and selected the lowest frequency for Ω_a. The main source of bandwidth limitation was determined to be the structural dynamics, which was suggested to be about 40 rad/s for fighter-like aircraft sized similarly to the X-29. However, Refs. [26–29] report the first aeroelastic modes were higher than this value, starting at about 70 rad/s. This is corroborated by the notch filters in the linear models starting at 68 rad/s.

A second source of bandwidth limitation discussed was the sampling rate of the flight computer. It was suggested that the flight control computer ran at 80 Hz and could therefore reliably pass signals up to about 30 or 40 rad/s [9, 10]. Although the computer ran at 80 Hz, it alternated between the longitudinal and lateral-directional axes, so that each control law had an effective rate of 40 Hz [23, 26, 29]. This rate has a Nyquist frequency of 20 Hz or about 126 rad/s, which is sufficient for control based on standard rules of thumb based on the dynamics of interest [30, 31].

The effects of actuator dynamics were also discussed. The model given for the command to stabilator deflection in Refs. [26] is

$$\frac{\delta(s)}{\delta_c(s)} = 0.885\left(\frac{20.2}{s+20.2}\right)\left[\frac{71.4^2}{s^2+2(0.736)(71.4)s+71.4^2}\right]\left(\frac{144.9}{s+144.9}\right) \tag{13}$$

where the pole at 20.2 rad/s is associated with the actuator ram dynamics and the higher-frequency poles model the electro-mechanical dynamics of the actuator. It was suggested in Refs. [9, 10] that the higher-frequency poles starting at 71.4 rad/s served as the limiting bandwidth for the actuators. Therefore, dynamics of the actuators, as well as other high-frequency dynamics including unsteady aerodynamics and sensor dynamics, were therefore not considered to be limiting factors for obtaining Ω_a.

For another perspective on determining the available bandwidth, consider Fig. 5, which surveys Model 4 in Table 2. This model, which is shown as a block diagram with continuous-time elements in Fig. 5(a), is one of the simpler models. The primary feedback is the sensed pitch rate, which is passed through notch filters and a second-order lead network before combining with the filtered pilot stick command and the PI compensation.

Figure 5(b) shows Bode plots of $L(s)$ for Model 4, presented in stages as a build-up of the full dynamics. The blue lines, which are labeled the nominal dynamics, represent the open-loop transfer function including the PI compensator, mixer, actuators, and bare airframe, i.e., from the tracking error $e(t)$ to pitch rate $q(t)$. The red lines in Fig. 5(b), which are labeled the parasitic dynamics, include the nominal dynamics, as well as the pitch rate sensor and notch filters. The main effect of adding the parasitic dynamics on the frequency range shown is an increase in phase lag at lower frequencies, which reduces the phase margin at 7.6 rad/s from 40.1 deg to 25.2 deg. To recover phase margin, adjust the crossover frequency, and achieve sufficient flying qualities, a second-order lead network and gain were added to the feedback path, which is shown by the green lines in Fig. 5(b). This additional lead increased the phase margin to 39.2 deg at 9.1 rad/s.

Figure 5(c) shows the corresponding sensitivity magnitudes using the same colors as in Fig. 5(b). Based on fitted prototypes to the sensitivity magnitudes, which are discussed next in Section III.E, the nominal loop had an available bandwidth of about 25 rad/s. From the above discussion, this bandwidth was mostly due to the first-order actuator pole near 20 rad/s. With the added parasitic dynamics, the peak sensitivity increased and the available bandwidth decreased to about 16 rad/s. After also including the lead network, the peak sensitivity decreased and the available

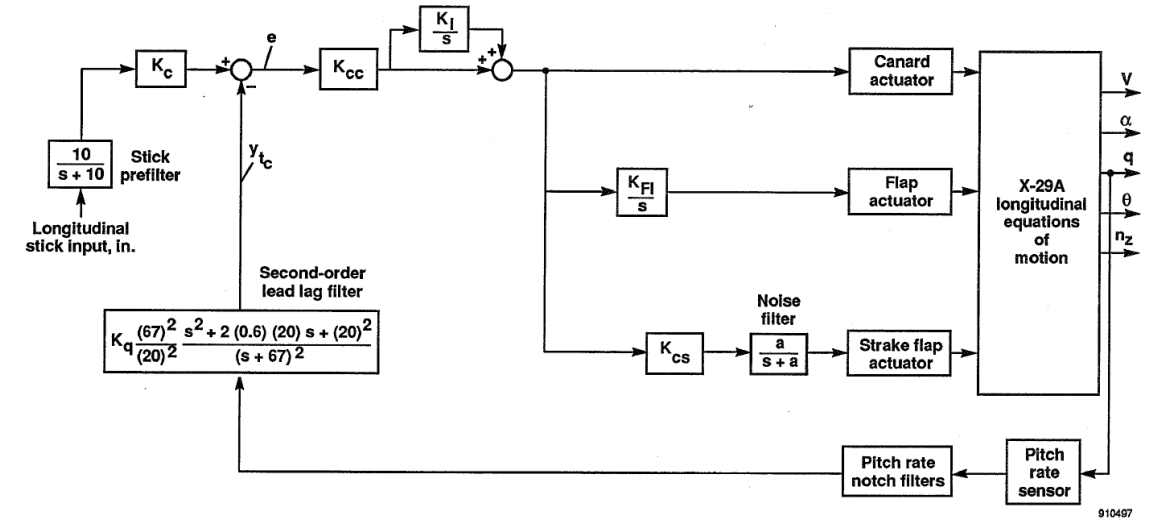

(a) System block diagram from Ref. [26]

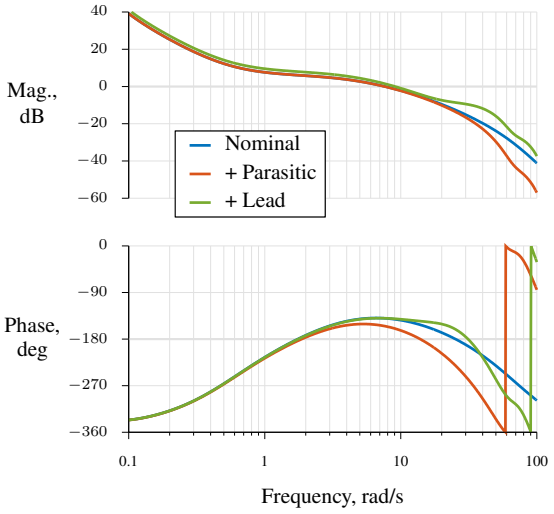

(b) Open-loop transfer function, $L(s)$

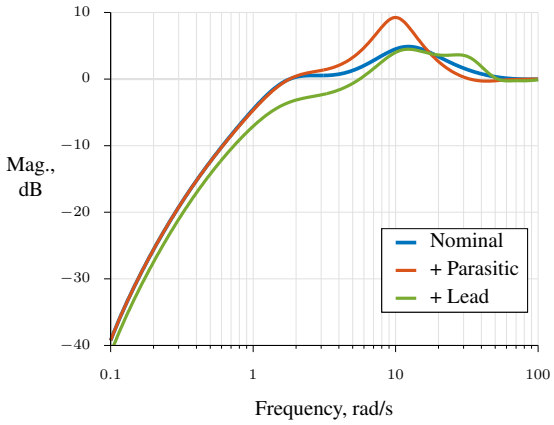

(c) Sensitivity transfer function, $S(s)$

Fig. 5 Control architecture and frequency responses, X-29 Model 4.

bandwidth increased to about 40 rad/s, which was the value selected for the available bandwidth [9, 10]. In all three cases, integrating the log sensitivity magnitude from 10^{-10} to 10^5 rad/s with 10^5 logarithmically spaced frequencies produced the value 9.5872, which is the same as 3.0517π to the number of decimal places shown, confirming Eq. (8).

In summary, an examination of NASA documentation and linear models of the closed-loop dynamics showed that the 40 rad/s value selected for the X-29 available bandwidth in Refs. [9, 10] was appropriate. However, that value seems to not be due to limitations from structural dynamics (based on the notch filter design and other documentation) and the computer sampling rate, as reasoned in Refs. [9, 10], but primarily from interactions between the actuator dynamics and the control law. As a result, the effective value of Ω_a depends on the control law, especially when there is dynamic compensation present, and not just the vehicle size and hardware, as proposed in Refs. [9, 10]. The terminology of an effective available bandwidth could be used to include the impact of feedback control on the system bandwidth.

E. Estimating the Available Bandwidth

Knowing now that the effective available bandwidth for the X-29 comes from the actuators and control law, the question remains about how that value would have been accurately determined in the first place, so that the approach

can be applied to other aircraft, especially those with dynamic compensation. If that question were posed during the conceptual design of the aircraft, before detailed models of the system and control law were available, the 20 rad/s actuator pole should probably have been used as the value. Note that the X-29 actuators came from the F-16 production aircraft and were well characterized. This assumption would have been conservative, per the discussion in the previous section, and would have led to conclusions about the X-29 robustness metrics that were too pessimistic or low.

If that question were instead posed after a linear model of the system was available, prototype functions could be fit to the sensitivity magnitude data. This idea was suggested by Stein in Ref. [9]. One approach for this is to fit the ideal prototype function from Eq. (11) to the sensitivity magnitude of the linear model. This was done by iterating on the two parameters Ω_1 and Ω_a using the Nelder-Mead simplex algorithm to minimize the least-squares error on the Bode magnitude plot

$$J = \frac{1}{2}\sum_{k=1}^{N} \nu^2(j\omega_k) \tag{14}$$

where

$$\nu(j\omega_k) = 20\log_{10}|S(j\omega_k)| - 20\log_{10}|\hat{S}(j\omega_k)| \tag{15}$$

is the fit error or residual and N is the number of frequencies used. The sensitivity magnitudes were sampled at 1000 points that were equally spaced on a logarithmic scale from 0.1 to 100 rad/s. To ensure the prototype function accurately reflected the robustness of the sensitivity function in terms of the stability margin, the prototype function was constrained to have the same peak value as the the linear model. Figure 6 shows the sensitivity magnitude for Model 4 as the blue line. The red line is the fitted model using the ideal prototype function.

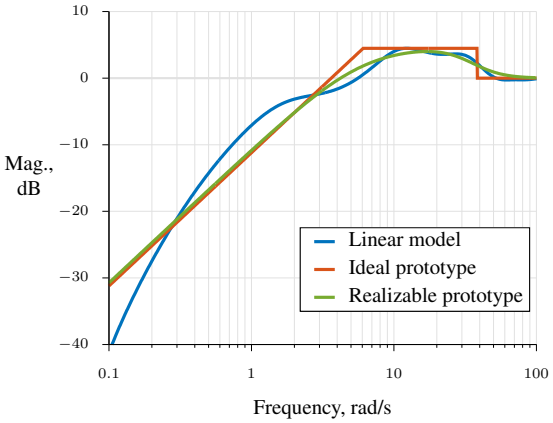

Fig. 6 Sensitivity function and fitted prototype functions, X-29 Model 4.

Stein also suggested approximating the ideal prototype function with the transfer function

$$S(s) \simeq \left(\frac{s}{s+\Omega_1}\right)\left(\frac{s^2+\sqrt{2}\Omega_a s+\Omega_a^2}{s^2+\sqrt{2}\Omega_2 s+\Omega_2^2}\right)\left(\frac{s-p_u}{s+p_u}\right) \tag{16}$$

which smooths the slope discontinuities and makes the prototype function realizable. The drawback of this approach is that the realizable prototype is not easily constrained to have the same peak value as the linear model. The new parameter Ω_2 provides roll-off to the sensitivity function after the maximum value is reached. The last term involving p_u contributes to the phase, and can be neglected if only the sensitivity magnitude is fit, as was done here. Additional factors can be included in Eq. (16) to improve the fitting ability, if desired [32]. In Fig. 6, the green line shows the fitted model using Eq. (16) and least squares.

This fitting process was performed for all six linear models using both the ideal and realizable prototype functions. Estimates for the identified parameters are given in Table 3. In general, the fits matched the high-order sensitivity functions well. The only exception to this was for Model 2, which was not fit well by either of the two prototype functions and had estimated parameters not in agreement with other models. This model is for the backup analog reversion system in the powered approach condition, which is a challenging control problem. Estimates of Ω_1 were close between the two fitted prototypes, whereas larger differences were seen in the estimate of Ω_a. One reason for

this is the extra parameter Ω_2 that is somewhat correlated with Ω_a. The other reason for this is that, as discussed in Section III.D, the effective Ω_a depends also on the control system, which differs between most of these linear models.

Table 3 Estimated parameters from fitting sensitivity magnitude functions

Model	Ideal Prototype			Realizable Prototype			
	$\hat{\Omega}_1$, rad/s	$\hat{\Omega}_a$, rad/s	J	$\hat{\Omega}_1$, rad/s	$\hat{\Omega}_2$, rad/s	$\hat{\Omega}_a$, rad/s	J
1	3.10	37.7	2163	3.07	26.3	30.9	2148
2	0.94	16.2	2317	2.32	7.42	9.91	2665
3	6.76	29.7	3818	6.30	27.3	36.5	3200
4	6.06	38.3	4149	5.94	31.9	40.7	3625
5	12.6	30.2	5773	10.3	28.4	43.6	4766
6	6.46	38.7	6124	7.45	28.4	42.7	6162

The variability of results in Table 3 from variations in the dynamics and control system between models suggests possible room for improvement in predicting fundamental limitations in robustness for the X-29. A different approach is to plot the unstable poles against the peak sensitivity values for each linear model, as in Fig. 4(b), and then fit Eq. (12c) to this data to determine estimates of Ω_1 and Ω_a. This is shown in Fig. 7 for the six linear models in Table 2. Lines and markers from Fig. 4(b) are copied over in green, for reference. The blue markers correspond to the six linear models. Note that Models 1 and 2 have essentially the same pole and peak sensitivity. The red lines are discussed below. Comparing the data and trends given by Stein and shown in green with the linear models in blue, the X-29 appears less robust than reported in Refs. [9, 10].

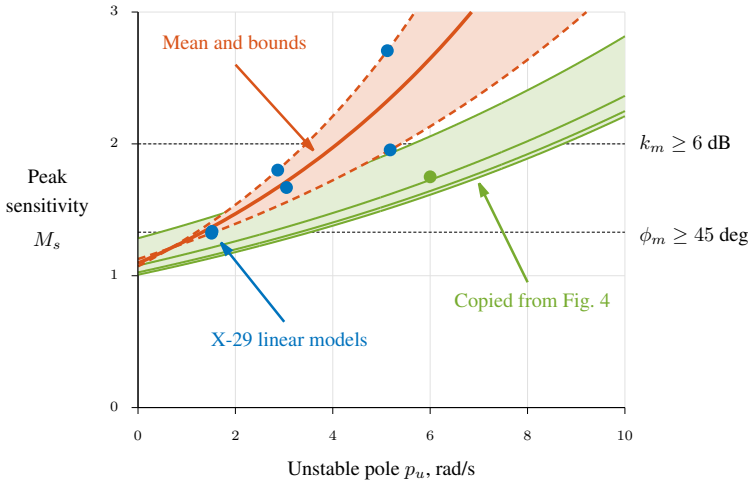

Fig. 7 X-29 peak sensitivities.

In general, results from different linear models appear as scattered data in Fig. 7, rather than falling along a single line given by Eq. (12c), due to variations in the plant dynamics with flight condition, as well as control law configuration changes and gain scheduling. To provide a quantitative measure of the robustness achieved by the collection of linear models, parameters in Eq. (12c) were estimated three ways. In the first approach, parameters Ω_1 and Ω_a were estimated to fit all the data from the linear models and produce an average trend, which is shown as the solid red line. This result gives an average view of the robustness trend. The other two fits, shown as the dashed red lines, were made to bound the data from above and below. The lower bounds limit the best-case robustness, whereas the upper bounds limit the worst-case robustness; both of which are useful for control design. Estimated parameters are given in Table 4.

In summary, this section examined different ways to estimate the available bandwidth for an aircraft control loop. Rough estimates can be obtained from knowledge of the hardware and relevant dynamics. Refined estimates can be obtained from fitting a sensitivity magnitude diagram with prototype functions. As the sensitivity functions can vary

Table 4 Estimated parameters from fitting X-29 peak sensitivity data

Fit	$\hat{\Omega}_1$, rad/s	$\hat{\Omega}_a$, rad/s
Upper bound	1.19	17.3
Mean line	1.94	21.4
Lower bound	3.52	29.5

significantly with flight condition, control architecture, and other factors, another approach is to bound the characteristics to determine the best-case achievable robustness.

IV. Analysis of the X-59 Aircraft

This section discusses the application of the Bode sensitivity integral to the robustness limitations of the X-59 LBFD aircraft. It will be shown that the direct analysis from Refs. [9, 10] does not lead to a clear picture of the robustness limitations for this aircraft, and that rather only a lower bound on the peak sensitivity can be determined from available linear models.

The stabilator is the primary control effector for pitch control. This surface is moved using the same actuator in the X-59 as was used in the X-29 and in production F-16 aircraft. The pitch-axis control law is a standard n_z-command system with proportional and integral terms [33, 34]. Supplemental damping and lead is supplied from additional feedback due to pitch rate and pitch acceleration, respectively. Gains are scheduled according to the flight condition. Based on this information and the X-29 analysis in the previous section, one might (incorrectly) surmise the available bandwidth could be about 25 rad/s, and the performance bandwidth again could be somewhere between 1 to 10 rad/s.

A nonlinear, rigid-body, six degree-of-freedom (DOF) flight dynamics simulation of the X-59 was constructed in MATLAB® and Simulink® by Lockheed Martin with input from NASA. This nonlinear simulation was numerically linearized at 1303 points over the flight envelope for various speeds, altitudes, weights and mass distributions, and settings for flaps and landing gear. The maximum Mach number analyzed was 1.7, the maximum altitude was 60,000 ft, and the weight ranged from 17,500 to 24,300 lbf.

Figure 8 shows contours of four variables over the Mach and altitude flight envelope that will be discussed more below. In these plots, the analyzed flight conditions are the red dots, and data at these points were interpolated to form the contour lines. Results are only shown for the 203 flight conditions at the mid-weight / aft-CG configuration with flaps at zero deflections and landing gear stowed. This subset contains the most unstable configurations in the pitch axis. The results discussed in the remainder of this paper only use these analysis points.

Figure 8(a) shows the unstable pole from the short period mode. In terms of the worst-case condition, the X-59 is about half as unstable as the X-29, with a pole at about +3.1 rad/s. However, the control design is not significantly easier for the X-59 because the structural dynamics are about half as fast, starting around 33 rad/s. The consequence of this is a tighter frequency range in which control of the rigid-body dynamics can be performed, which prohibits the relatively simple solution used for the X-29 analog reversion design in Fig. 5(a) of adding lead to the feedback loop to improve robustness and flying qualities.

Figure 9 shows a Bode magnitude plot of the sensitivity function for the design point at Mach 1.39, altitude 52,300 ft, mid-weight / aft-CG up-and-away configuration. The blue line is the high-order sensitivity function from the linearized model. This sensitivity plot has a similar shape to that of the X-29 shown in Fig. 6. Some differences include a slower roll-off at low frequencies and the more pronounced effect of the notch filters at high frequencies. More importantly for the robustness analysis, Fig. 9 shows a higher peak value and a steeper curve around that point. From the left side, the loop shape is constrained by the flying qualities metrics used to design the flight control system. From the right side, the loop shape is constrained by the actuator pole and the structural dynamics. The higher peak value is a result of the vehicle instability and the narrow band in which sensitivity is added.

Also shown as the red and green lines in Fig. 9 are the ideal and realizable fitted prototype functions, respectively. The fitted ideal prototype function had estimates $\hat{\Omega}_1 = 8.19$ and $\hat{\Omega}_a = 15.7$ rad/s. Although the low frequencies are fit well and the peak value is matched, the estimated available bandwidth is too low. This is because a least-squares cost function was used and the notch filters created dips in the sensitivity below 1 or 0 dB at higher frequencies. The discontinuity in the fitted prototype between the low-frequency and high-frequency regions near 8 rad/s is due to constraining the prototype to have the same peak value as the higher-order sensitivity magnitude, as mentioned

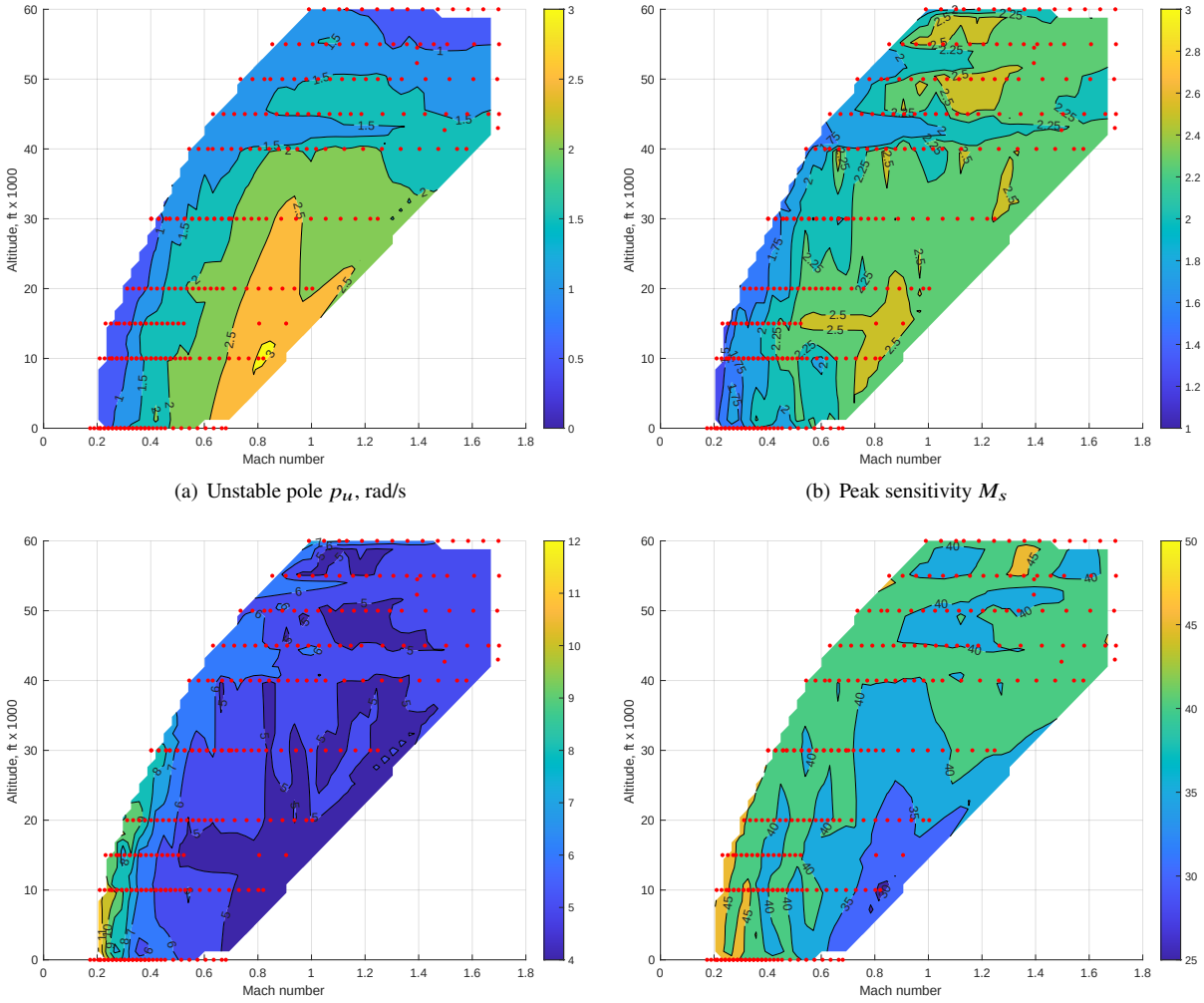

(a) Unstable pole p_u, rad/s

(b) Peak sensitivity M_s

(c) Minimum gain margin absolute value, $|k_m|$, dB

(d) Minimum phase margin ϕ_m, deg

Fig. 8 X-59 flight envelope contours for the mid-weight / aft-center of gravity configuration with flaps at zero deflection and landing gear stowed.

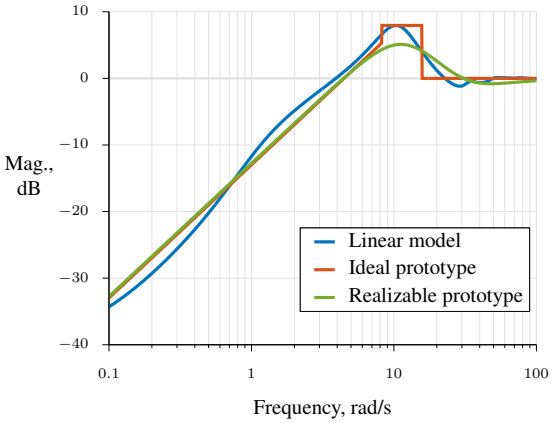

Fig. 9 Sensitivity function and fitted prototype functions, X-59 design point.

in Section III.E. The fitted realizable prototype function had estimates $\hat{\Omega}_1 = 30.8$, $\hat{\Omega}_2 = 11.7$, and $\hat{\Omega}_a = 31.1$ rad/s. Although the low-frequency region was again fit well, the peak sensitivity was not well captured and the available bandwidth estimate was too high. Also, the sharper peak and notch filters resulted in estimates where $\hat{\Omega}_1 > \hat{\Omega}_2$, which does not reflect the intended shape of the prototype function. Therefore, fitting individual sensitivity plots again did not accurately reflect robustness limitations of the X-59.

Figure 10 shows the peak sensitivity values as a function of the unstable pole. The axes in this plot were set to the same scales as for the X-29 plots. The blue circles are values obtained from interrogating the sensitivity functions of the 203 linear models. The green lines and shaded region show Eq. (12c) with an available bandwidth of 25 rad/s and a performance bandwidth ranging from 1 to 10 rad/s. It is clear from this plot that the trend of the linear models is not captured by this data, and is optimistic in terms of the robustness that can be achieved. The solid red line shows a fitted mean trend line using Eq. (12c), and had estimates $\hat{\Omega}_1 = 13.0$ and $\hat{\Omega}_a = 23.3$ rad/s. The dashed red lines show fits that bound the data from below and above, which had estimates of $\hat{\Omega}_1 = 2.1$ and $\hat{\Omega}_a = 13.9$ rad/s, and $\hat{\Omega}_1 = 19.4$ and $\hat{\Omega}_a = 23.0$ rad/s, respectively.

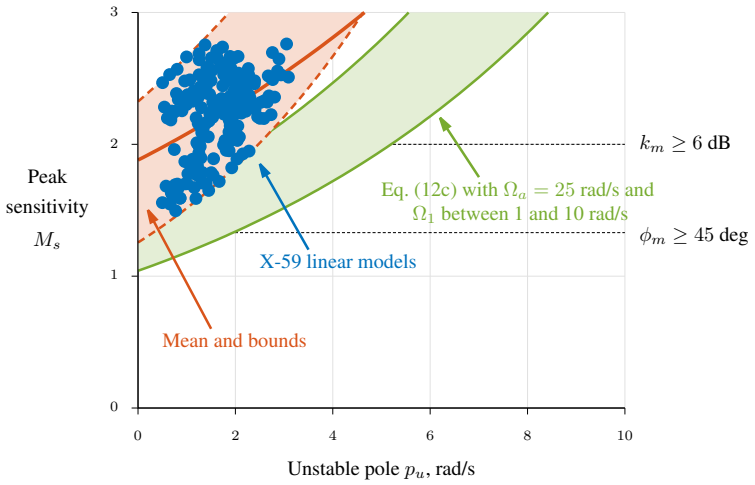

Fig. 10 X-59 peak sensitivities.

Note again that the horizontal lines and 2.0048 and 1.3066 are minimum bounds on the gain and phase margins, and that the actual margins can be significantly larger. Figure 8(b) shows contours of M_s over the flight envelope from the high-order linear models, and Figs. 8(c) and 8(d) show the minimum gain and phase margins. Figure 8(c) shows the absolute value of the gain margin because the limiting case switches between the negative low-frequency margin k_{m_1} and the positive high-frequency margin k_{m_2}. Despite the pessimistic outlook given by Fig. 10, the gain and phase margins, as well as the peak sensitivity values, were acceptable. In addition to checking SISO margins at the actuators, other analyses calculating these margins at the sensor outputs and using MIMO techniques did not indicate a collapse in robustness.

In summary, this section applied an analysis using the Bode sensitivity integral to the X-59 LBFD. Assumptions on the available bandwidth from knowledge of the hardware alone produced results that were too optimistic and had better robustness characteristics than implied by the linear models. Fitting individual sensitivity functions also resulted in inaccurate estimates of closed-loop robustness. Trends and bounds were fit to a collection of high-order linear models that showed difficulty meeting traditional gain and phase margin specifications. However, interrogating the linear models directly for gain and phase margins showed the robustness was adequately met.

V. Conclusions

This paper discussed the robustness limitations of unstable aircraft as viewed from the perspective of the Bode sensitivity integral. This integral reflects the fundamental tradeoff between performance and robustness, and shows how robustness analysis for systems with characteristics such as unstable open-loop poles is hindered. In his presentation for the first IEEE CSS Hendrik W. Bode Lecture Prize, Gunter Stein used the Bode sensitivity integral to illustrate fundamental limitations in robustness for the X-29 aircraft. In this paper, that analysis was revisited, modified, and

applied to another unstable aircraft, the X-59 low-boom flight demonstrator.

The contributions and findings of this paper can be summarized as the following:

1) The limiting source of the 40 rad/s available bandwidth for the X-29, which was previously attributed to structural modes and digital sampling effects, was identified as the interaction between the 20.2 rad/s actuator pole and lead compensation in the feedback path.
2) It was shown that the available bandwidth parameter Ω_a not only depends on the aircraft hardware, but also depends on the control system design. Lead compensation in the X-29 flight control law extended the effective value of the parameter from about 25 to 40 rad/s.
3) Fitting sensitivity magnitudes with prototype functions generally did not accurately reflect robustness.
4) In working through the X-29 example and then to the X-59 airplane, Stein's analysis gave useful insights into control design limitations but was generally found to be too imprecise to provide accurate limitations of robustness for control design. Rather, conventional analyses using linearized models, SISO and MIMO robustness analyses, Monte Carlo simulations, and other techniques are still preferred.
5) The plot of the unstable pole vs. peak sensitivity over the flight envelope appears as a point cloud for aircraft due to changes in plant dynamics and control laws with flight condition. It was proposed to fit these data with curves that capture the mean trend and bound the ranges, which quantifies the average, best-case, and worst-case robustness achieved.

Acknowledgments

This research was supported by the NASA Low-Boom Flight Demonstrator (LBFD) project, which is part of the NASA Integrated Aviation System Program (IASP). Contributions by the X-59 team members at NASA Armstrong Flight Research Center (AFRC), NASA Langley Research Center (LaRC), and Lockheed Martin Aeronautics are gratefully acknowledged. Dr. David Cox of NASA LaRC generated the linearized models of the X-59 from the nonlinear simulation developed by Mr. Jason Oubre and Mr. Nicholas Vazquez of Lockheed Martin Aeronautics. Technical conversations with Dr. Barton Bacon of NASA LaRC are acknowledged and appreciated. Dr. Jeffrey Ouellette of NASA LaRC helped to locate documentation related to the X-29.

References

[1] Gipson, L., "Quesst," `https://www.nasa.gov/mission/quesst`, accessed Apr. 2024.

[2] Townsend, J., and Raymond, E., "Background Information and User Guide for MIL-F-9490D: Flight Control Systems — Design, Installation and Test of Piloted Aircraft, General Specification for," U.S. Air Force report AFFDL-TR-74-116, Jan. 1975.

[3] Anon., "Flight Control Systems — Design, Installation and Test of Piloted Aircraft General Specification for," US Department of Defense MIL-F-9490D, Sep. 2007.

[4] Anon., "Flying Qualities of Piloted Aircraft," US Department of Defense MIL-STD-1797B, Apr. 2012.

[5] Anon., "Vehicle Management Systems — Flight Control Function, Design, Installation and Test of Piloted Military Aircraft, General Specification for," SAE International AS94900A, Aug. 2018.

[6] Enns, D., Wall, J., Hendrick, R., and Ginter, S., "Analysis of the Flight Control Laws for the Forward Swept Wing Aircraft," NASA CR-166621, Oct. 1986.

[7] Chin, J., Chacon, V., and Gera, J., "X-29A Flight Control System Performance During Flight Test," AIAA Paper 87-2878, Sep. 1987. doi:10.2514/6.1987-2878.

[8] Clarke, R., Burken, J., Bosworth, J., and Bauer, J., "X-29 Flight Control System: Lessons Learned," NASA TM-4598, June 1994.

[9] Stein, G., "Respect the Unstable," presentation for the first IEEE CSS Hendrik W. Bode Lecture Prize, 1989.

[10] Stein, G., "Respect the Unstable," *IEEE Control System Magazine*, Vol. 23, No. 4, Aug. 2003, pp. 12–25. doi:10.1109/MCS.2003.1213600.

[11] Bode, H., *Network Analysis and Feedback Amplifier Design*, D. Van Nostrand Company, New York, NY, 1945.

[12] Åström, K., and Murray, R., *Feedback Systems: An Introduction for Scientists and Engineers*, 2nd ed., Princeton University Press, Princeton, NJ, 2021.

[13] Ogata, K., *Modern Control Engineering*, Prentice-Hall, Englewood Cliffs, NJ, 1970.

[14] Maciejowski, J., *Multivariable Feedback Design*, Addison-Wesley, Wokingham, England, 1989.

[15] Schmidt, D., *Modern Flight Dynamics*, AIAA, Reston, VA, 2023.

[16] Sanner, R., "Control of Aerospace Systems," course notes for ENAE432, University of Maryland, 2021.

[17] Lebsock, K., "Fundamentals of Linear Stability," NASA Engineering and Safety Center (NESC) Academy webcast, `https://nescacademy.nasa.gov`, Oct. 2014.

[18] Šebek, M., and Hurák, Z., "An Often Missed Detail: Formula Relating Peek Sensitivity with Gain Margins Less than One," 17th International Conference on Process Control, Le-We-2, 115, Jun. 2009.

[19] Skogestad, S., and Postlethwaite, I., *Multivariable Feedback Control*, 3rd ed., John Wiley & Sons, Hoboken, NJ, 2005, pp. 163–219.

[20] Freudenberg, J., and Looze, D., "Right Half Plane Poles and Zeros and Design Tradeoffs in Feedback Systems," *IEEE Transactions on Automatic Control*, Vol. 30, No. 6, June 1985, pp. 555–565. doi:10.1109/TAC.1985.1104004.

[21] Ruth, M., Lebsock, K., and Dennehy, C., "What's New is What's Old: Use of Bode's Integral Theorem (circa 1945) to Provide Insight for 21st Century Spacecraft Attitude Control System Design Tuning," AIAA Paper 2010-8428, Aug. 2010. doi:10.2514/6.2010-8428.

[22] Lavretsky, E., and Wise, K., "Bode's Integral Theorem and Flight Control," AIAA Paper 2024-0722, Jan. 2024. doi: 10.2514/6.2024-0722.

[23] Whitaker, A., and Chin, J., "X-29 Digital Flight Control System Design," AGARD CP-384, Oct. 1994.

[24] McRuer, D., Ashkenas, I., and Graham, D., *Aircraft Dynamics and Automatic Control*, Princeton University Press, Princeton, NJ, 1973.

[25] Morelli, E., and Klein, V., *Aircraft System Identification: Theory and Practice*, 2nd ed., Sunflyte Enterprises, Williamsburg, VA, 2016.

[26] Bosworth, J., "Linearized Aerodynamic and Control Law Models of the X-29A Airplane and Comparison With Flight Data," NASA TM-4356, Feb. 1992.

[27] Clarke, R., "Working with Matlab/Simulink Examples from NASA TM-4356," ResearchGate `https://www.researchgate.net`, accessed Apr. 2024.

[28] Gera, J., Bosworth, J., and Cox, T., "X-29A Flight Test Techniques and Results: Flight Controls," NASA TP-3121, May 1991.

[29] Kehoe, M., Laurie, E., and Bjarke, L., "An In-Flight Interaction of the X-29A Canard and Flight Control System," AIAA Paper 90-1240, Apr. 1990. doi:10.2514/6.1990-1240.

[30] Lewis, F., *Applied Optimal Control and Estimation: Digital Design and Implementation*, Prentice Hall, Englewood Cliffs, NJ, 1992.

[31] Franklin, G., Powell, J., and Workman, M., *Digital Control of Dynamic Systems*, 3rd ed., Ellis-Kagle Press, Half Moon Bay, CA, 1998.

[32] Cho, N., and Lee, H., "Approximation of Achievable Robustness Limit Based on Sensitivity Inversion," *Journal of Guidance, Control, and Dynamics*, Vol. 47, No. 1, Jan. 2024, pp. 143–155. doi:10.2514/1.G007169.

[33] Stevens, B., Lewis, F., and Johnson, E., *Aircraft Control and Simulation*, 3rd ed., John Wiley & Sons, Hoboken, NJ, 2016.

[34] Lavretsky, E., and Wise, K., *Robust and Adaptive Control: With Aerospace Applications*, 2nd ed., Springer, Cham, Switzerland, 2024.